

LUMINA: A Grid Foundation Model for Benchmarking AC Optimal Power Flow Surrogate Learning

Hongwei Jin¹, Keunju Song², Zeeshan Memon³, Yijiang Li¹, Stefano Fenu⁴, Hongseok Kim², Liang Zhao³, and Kibaek Kim¹

¹Mathematics and Computer Science Division, Argonne National Laboratory

²Department of Electronic Engineering, Sogang University

³Department of Computer Science, Emory University

⁴Energy Systems and Infrastructure Assessment Division, Argonne National Laboratory

May 5, 2026

Abstract

AC optimal power flow (ACOPF) is foundational yet computationally expensive in power grid operations, driving learning-based surrogates for large-scale grid analysis. These surrogates, however, often fail to generalize across network topologies, a critical gap for deployment on grids not seen during training and for routine operational what-if studies. We introduce LUMINA-Bench, a comprehensive benchmark suite for ACOPF surrogate learning covering multi-topology pretraining, transfer, and adaptation. The benchmark evaluates homogeneous and heterogeneous architectures under single- and multi-topology learning settings using unified metrics that capture both predictive accuracy and physics-informed constraint violations. We additionally compare constraint-aware training objectives, including MSE, augmented Lagrangian, and violation-based Lagrangian losses, to characterize accuracy–robustness trade-offs across settings. Data processing, training, and evaluation frameworks are open-sourced as the LUMINA suite to support reproducibility and accelerate future research on feasibility-aware OPF surrogates.

1 Introduction

AC optimal power flow (ACOPF) is a foundational optimization primitive in power system operations, used to determine economically optimal generator dispatch while satisfying physical and operational constraints across a network [6, 23, 10, 11]. Two practical challenges limit its use at scale. First, modern grid analysis increasingly demands massive what-if studies, encompassing millions of contingency scenarios in reliability assessments and diverse operating conditions in planning, where ACOPF must be solved repeatedly. Second, ACOPF is nonconvex and nonlinear, typically requiring tailored iterative optimization procedures with prohibitive runtime for large systems. These computational bottlenecks have motivated both hardware-accelerated nonlinear optimization (e.g., [31, 27, 24, 32, 17, 19]) and learning-based surrogates (e.g., [28, 16, 29, 38, 9, 14]).

Learning-based surrogates offer a compelling alternative by amortizing computational cost through offline training, enabling near-instantaneous inference at deployment; more broadly, this direction aligns with emerging efforts on foundation-model perspectives for power grids [13]. Recent surrogates can be broadly grouped by model class and how they leverage network structure. Deep neural networks (DNNs) learn direct mappings from operating conditions to optimal solutions (or subsets thereof), including DeepOPF [28] and DeepOPF-V [16], with extensions to augmented load conditions [29]. While DNNs can yield strong speedups, graph neural networks (GNNs) have emerged as a natural choice for handling topology and locality, by exploiting the grid’s graph structure via message-passing [12, 20, 30]. Existing GNN-based surrogates include homogeneous architectures that treat all nodes uniformly [26, 8, 18, 35, 33, 37] and heterogeneous architectures that explicitly distinguish component types (e.g., buses, generators, loads) [15, 22, 39, 5].

Beyond architecture, constraint handling is central for ACOPF surrogates because feasibility with respect to power flow physics and operational limits is non-negotiable in downstream use. Mean squared error (MSE) captures prediction fidelity to optimal solutions but does not directly enforce feasibility. Augmented Lagrangian (AL) methods [4] incorporate constraints into training objectives, while violation-based Lagrangian (VBL) methods [9] explicitly penalize constraint violations in the loss. Alternative directions include post-inference correction [34], loss constructions derived from KKT conditions [25, 7], and feasibility-oriented architectures for learning constrained ACOPF solutions [38, 14]. As emphasized in prior work, evaluating ACOPF surrogates require multiple dimensions: predictive accuracy on in-distribution operating points, generalization to unseen operating conditions and topologies [36], scalability across grid sizes, and constraint satisfaction to ensure operational feasibility. However, a systematic benchmark that standardizes tasks, data splits, feasibility metrics, and hyperparameter optimization (HPO) budgets, while evaluating representative baseline architectures and constraint-aware objectives across these dimensions, remains missing.

LUMINA (**L**arge-scale **U**nified **M**odel for **I**ntelligent grid **A**pplications) is our grid foundation model effort for learning fast, physics-consistent surrogates for ACOPF and related grid optimization primitives. To support systematic and reproducible evaluation, we introduce LUMINA-Bench, a benchmark suite for learning and evaluating ACOPF surrogates across single-topology, multi-topology pretraining, and transfer/adaptation settings. LUMINA-Bench builds on OPFData [21], which provides ACOPF solutions on multiple representative network topologies and diverse operating points. Using standardized protocols, our benchmark suite evaluates a curated baseline set of homogeneous and heterogeneous GNN architectures under matched HPO budgets, and compares widely used constraint-aware training objectives (AL and VBL, as well as MSE). Crucially, LUMINA-Bench reports topology-invariant feasibility metrics that quantify physical validity (e.g., power balance and line-limit violations) alongside predictive error, enabling comparisons across grid sizes and topologies.

Contributions. (i) **Benchmark task suite.** We define standardized benchmark tasks for ACOPF surrogate learning spanning single-topology training, multi-topology pretraining, and transfer/adaptation, with fixed data splits and evaluation protocols based on OPFData [21]. (ii) **Baseline suite under matched budgets.** We provide a representative baseline set of homogeneous and heterogeneous architectures and compare constraint-aware objectives (AL, VBL) under matched hyperparameter optimization budgets. (iii) **Generalization and transfer evidence.** We report results that characterize in-distribution performance, transfer learning, and (where applicable) zero-shot generalization across held-out topologies and larger networks using unified feasibility metrics. (iv) **Open-source reproducibility.** We release reproducible data processing, training, and evaluation pipelines as the LUMINA-Bench suite to support research on feasibility aware ACOPF surrogates.

2 LUMINA-Bench Definition

This section formalizes LUMINA-Bench by specifying the benchmark tasks, the underlying dataset and topology selection, the ACOPF problem setup, a unified graph I/O schema, and evaluation metrics that jointly capture accuracy and feasibility.

2.1 Tasks and Protocol

LUMINA-Bench organizes evaluation into four tasks that stress complementary aspects of ACOPF surrogate learning.

T1: Single-topology training. Train and evaluate on a single network topology with disjoint train/validation/test operating points. This task measures in-distribution accuracy and feasibility when the topology is fixed.

T2: Multi-topology pretraining. Train a single model jointly on multiple topologies and evaluate on the same set of topologies. This task measures whether a shared model can capture common structure across networks and improve sample efficiency relative to training separate models.

T3: Held-out topology generalization. Train on a subset of topologies and evaluate on an unseen topology that is withheld entirely from training. This task probes topology-shift generalization under the same OPF variable definitions and evaluation metrics.

T4: Transfer and adaptation. Pretrain a model using one or more source topologies (or smaller networks) and fine-tune using a limited amount of data from a target topology (or larger network). This task evaluates transferability and scaling behavior under matched fine-tuning budgets.

Across all tasks, we report prediction error and topology-normalized feasibility violations defined in Section 2.5.

2.2 Dataset and Topology Selection

We base LUMINA-Bench on OPFData [21], which provides solved ACOPF instances across ten representative power network topologies. For each topology, OPFData includes 300K feasible operating points obtained by perturbing load profiles and solving the corresponding ACOPF with a state-of-the-art solver. We use OPFData solutions as supervision and adopt fixed train/validation/test splits per topology to ensure consistent comparisons across tasks, models, and objectives.

Our benchmark uses case30, case57, case118, case500, and case2000. We use case30 primarily for hyperparameter optimization (HPO) and ablations; case57 and case118 for multi-topology training and held-out-topology evaluation; and case500 and case2000 to assess scaling behavior and fine-tuning on larger systems.

We use fixed train/validation/test splits per topology across all experiments; held-out-topology tasks withhold an entire topology (including validation), and transfer/adaptation fine-tunes on a limited subset of the target training split while reporting on the target test split.

2.3 AC Optimal Power Flow Problem

For a set of buses \mathcal{N} , generators \mathcal{G} , and transmission lines \mathcal{L} , ACOPF aims to minimize the total generation cost function $C(P_g)$:

$$C(P_g) = \sum_{g \in \mathcal{G}} (c_{2,g} P_g^2 + c_{1,g} P_g + c_{0,g}), \quad (1)$$

where P_g is the active power output of generator $g \in \mathcal{G}$, and $c_{2,g}$, $c_{1,g}$, and $c_{0,g}$ are cost coefficients, subject to a set of constraints on power balance, generation, voltage, and line flow as follows.

Power Balance Equations: The net active and reactive power injection at a given bus $i \in \mathcal{N}$ must equal the power flow out of the bus into the rest of the network:

$$\sum_{g \in \mathcal{G}_i} P_g - P_{d,i} = \sum_{j \in \mathcal{N}_i} P_{ij}(V, \theta), \quad \sum_{g \in \mathcal{G}_i} Q_g - Q_{d,i} = \sum_{j \in \mathcal{N}_i} Q_{ij}(V, \theta), \quad (2)$$

where $P_{ij}(V, \theta)$ and $Q_{ij}(V, \theta)$ are the standard AC branch-flow functions induced by the bus admittance matrix $Y_{ij} = G_{ij} + jB_{ij}$.

Generation Limits: Active and reactive power generation must be within the physical limits of each generator:

$$P_g^{\min} \leq P_g \leq P_g^{\max}, \quad Q_g^{\min} \leq Q_g \leq Q_g^{\max} \quad (3)$$

Voltage Limits: Voltage magnitudes and angles must remain within the operational bounds of each bus:

$$V_i^{\min} \leq V_i \leq V_i^{\max}, \quad \theta_i^{\min} \leq \theta_i \leq \theta_i^{\max} \quad (4)$$

Line Flow Limits: Power flow on a given transmission line must not exceed the line’s thermal ratings:

$$P_{ij}^2 + Q_{ij}^2 \leq (S_{ij}^{\max})^2. \quad (5)$$

Note that power flow equations (2) can be efficiently solved by traditional methods (e.g., Newton-Raphson); however, ACOPF is an NP-hard optimization problem [2] with inequality constraints (3)–(5). In LUMINA-Bench, surrogates take operating conditions and topology as input and predict ACOPF decision variables; feasibility is evaluated via the residuals of (2) and (5).

2.4 Graph-Based Input-Output Representation

We cast ACOPF surrogate learning as a graph-based operator learning problem, where the power grid is represented as a heterogeneous graph $G = (\mathcal{V}, \mathcal{E})$ and the surrogate learns a mapping from operating conditions to ACOPF solution variables.

Graph representation. The node set comprises four types (bus, generator, load, shunt); edges represent transmission/transformer connectivity with electrical parameters and thermal limits. Full node/edge feature definitions are provided in Appendix B.

Input schema. For a given operating point, the surrogate model receives as input the grid topology and component attributes encoded in the graph representation G , including load demand $(P_{d,i}, Q_{d,i})$. No ACOPF solution is provided as inputs.

Output schema. The surrogate predicts a subset of ACOPF solution variables $(V_i, \theta_i, P_g, Q_g)$ for all $i \in \mathcal{N}, g \in \mathcal{G}$. The prediction variables are normalized (via the corresponding min-max bounds) to satisfy the simple bound constraints (3)–(4). Accordingly, we report feasibility via residual norms of (2) and (5).

2.5 Evaluation Metrics

We evaluate all models using a common metric suite that captures predictive accuracy and physical feasibility.

Prediction accuracy. We report MSE between predicted and ground-truth ACOPF solution variables, evaluated on both seen and unseen topologies under each benchmark task. We also report accuracy as OPF solution error in tables and figures.

Constraint violation. We quantify physical feasibility by measuring violations of each constraint family induced by the prediction. For each constraint type $c \in \{\text{power balance, line flow limit}\}$, we compute a per-sample violation vector $v_c^{(s)}$ (stacking bus-wise residuals for power balance or line-wise residuals for flow limits) from the corresponding ACOPF residuals induced by $\hat{\mathbf{y}}$ (power-balance residuals from (2) and line-limit residuals from (5)). The violation for constraint type c is then defined as the ℓ_2 -norm of the per-sample violation vector, averaged over test samples: $\text{Viol}_c = \frac{1}{|\mathcal{S}|} \sum_{s \in \mathcal{S}} \|v_c^{(s)}\|_2$. To enable comparison across network sizes, we report a topology-normalized total violation score defined as the sum of per-type violations normalized by the square root of the number of buses N : $\text{Viol} = \frac{1}{\sqrt{N}} \sum_c \text{Viol}_c$. We use Viol as the primary feasibility metric throughout the paper, and additionally report Viol_c to diagnose which constraint families dominate infeasibility.

3 Baselines and Objectives

We define the baseline suite and training objectives used to validate LUMINA-Bench, covering representative homogeneous and heterogeneous graph architectures and constraint-aware losses under a fixed input/output schema.

3.1 Baseline Models

We consider eight representative GNN backbones that are commonly used in prior work on learning-based OPF surrogates and cover both homogeneous (single node/edge type) and heterogeneous (typed nodes/edges) message passing. All benchmark models share the same graph input/output schema (Section 2.4) but differ along two axes: (i) backbone architecture and (ii) whether grid heterogeneity (node/edge types) is encoded explicitly. All models produce node-level predictions that are assembled into the ACOPF solution vector, are trained under the same objectives (Section 3.2), and are evaluated with the same metrics (Section 2.5). We select widely used backbones that span (i) message passing vs attention and (ii) homogeneous vs typed (heterogeneous) graphs, to cover common OPF-surrogate design choices under a fixed I/O schema.

Homogeneous backbones. We include three widely used homogeneous message-passing architectures that treat all nodes and edges uniformly: **GCN** [18], **GAT** [33], and **GIN** [35]. These baselines operate on the graph adjacency and aggregate information from one-hop neighborhoods without explicit node/edge typing. We also include a **Graph Transformer** baseline that applies multi-head attention over graph neighborhoods (with adjacency-based masking) to capture longer-range interactions beyond standard message passing [37].

Heterogeneous backbones. To explicitly represent the heterogeneity of grid components (e.g., buses, generators, loads, shunts) and relational structure, we include four heterogeneous architectures: **RGAT** [5], **HeteroGNN** [39], **HGT** [15], and **HEAT** [22]. These methods use type-specific projections and/or relation-specific attention to enable different transformation and aggregation rules across node and edge types. In our setting, node types correspond to the component types in Section 2.4, and edge types correspond to physical connections (e.g., transmission lines and transformer relations), following the canonical heterogeneous graph formalism.

For completeness, we provide the explicit layer update equations used in our implementations in Appendix C.

3.2 Training Objectives

Let \mathbf{y} be the ground-truth ACOPF solution labels and $\hat{\mathbf{y}} = f_\theta(G)$ the model prediction. We define residual functions that measure constraint violations induced by $\hat{\mathbf{y}}$: (i) equality residuals $\mathbf{r}(\hat{\mathbf{y}})$ for (2), and (ii) inequality residuals $\mathbf{h}(\hat{\mathbf{y}}) \leq \mathbf{0}$ for (5).

Pointwise regression (MSE). The default objective minimizes squared error (MSE) on solution variables:

$$L_{\text{MSE}}(\theta) = \mathbb{E} [\|\hat{\mathbf{y}} - \mathbf{y}\|_2^2].$$

This objective measures predictive accuracy but does not explicitly enforce feasibility.

Augmented Lagrangian (AL). To encourage feasibility during training, we incorporate constraint residuals using an augmented Lagrangian objective [4] as follows:

$$\begin{aligned} L_{\text{AL}}(\theta; \boldsymbol{\lambda}, \boldsymbol{\mu}, \rho) &= L_{\text{MSE}}(\theta) + \boldsymbol{\lambda}^T \mathbf{r}(\hat{\mathbf{y}}) + \frac{\rho}{2} \|\mathbf{r}(\hat{\mathbf{y}})\|_2^2 \\ &\quad + \boldsymbol{\mu}^T \max\{\mathbf{h}(\hat{\mathbf{y}}), 0\} + \frac{\rho}{2} \|\mathbf{h}(\hat{\mathbf{y}})\|_2^2, \end{aligned}$$

where $\boldsymbol{\lambda}$ and $\boldsymbol{\mu}$ are dual variables associated with equality constraints and inequality constraints, respectively, and $\rho > 0$ is a penalty parameter. During the training for θ , $(\boldsymbol{\lambda}, \boldsymbol{\mu})$ are updated periodically using ascent steps with projection for nonnegativity:

$$\boldsymbol{\lambda} \leftarrow \boldsymbol{\lambda} + \rho \mathbf{r}(\hat{\mathbf{y}}), \quad \boldsymbol{\mu} \leftarrow \boldsymbol{\mu} + \rho \max\{\mathbf{h}(\hat{\mathbf{y}}), 0\}.$$

This objective adaptively reweights constraint satisfaction during training and typically reduces violations under distribution shift.

Violation-based Lagrangian (VBL). As a feasibility-aware alternative, we use violation-based Lagrangian objective [9] as follows:

$$L_{\text{VBL}}(\theta; \boldsymbol{\lambda}, \boldsymbol{\mu}) = L_{\text{MSE}}(\theta) + \boldsymbol{\lambda}^T |\mathbf{r}(\hat{\mathbf{y}})| + \boldsymbol{\mu}^T \max\{\mathbf{h}(\hat{\mathbf{y}}), 0\},$$

where $\boldsymbol{\lambda}, \boldsymbol{\mu} \geq 0$ are the Lagrangian multipliers that control the accuracy-feasibility trade-off. Similar to AL, the dual variables are updated periodically using ascent steps with step size $\rho > 0$:

$$\boldsymbol{\lambda} \leftarrow \boldsymbol{\lambda} + \rho |\mathbf{r}(\hat{\mathbf{y}})|, \quad \boldsymbol{\mu} \leftarrow \boldsymbol{\mu} + \rho \max\{\mathbf{h}(\hat{\mathbf{y}}), 0\}.$$

This objective adaptively weights constraint violation degrees, as compared to the satisfiability degree [9].

4 Experimental Protocol

This section describes the experimental protocol across all experiments in this paper.

4.1 Training and Hyperparameter Optimization

We employ a unified HPO and training protocol across the eight architectures to ensure fair comparison. All HPO is conducted on case30 using a fixed training budget of 2M samples seen per run. We use W&B Sweep with Bayesian method and hyperband-based early stopping, with a minimum resource of 600k samples-seen for pruning underperforming trials.

Model selection criterion. Each trial is evaluated on a validation set using a validation score that combines the prediction MSE and the total constraint violation, where the violation term is normalized by \sqrt{N} to reduce sensitivity to network size. At the end of each HPO stage, we select the configuration with the best (lowest) validation score ($= \text{MSE}_{\text{val}} + \text{Viol}_{\text{total, val}}/\sqrt{N}$).

Two-stage HPO. We propose a two-stage HPO. In stage 1, we tune architecture- and optimizer-related hyperparameters over a shared search space including learning rate, weight decay, dropout, hidden dimension, number of layers, batch size, and gradient clipping norm, using 50 trials per architecture. In Stage 2, we fix the best Stage-1 configuration each from the homogeneous and heterogeneous architecture groups and then sweep hyperparameters specific to Lagrangian-based objectives, covering both the augmented Lagrangian (AL) and violation-based Lagrangian losses.

Across all runs and both stages, we train with AdamW and apply gradient clipping using the tuned clipping norm. We leave the full hyperparameter settings and discuss observations during HPO in Appendix D.

4.2 Implementation Invariants

To isolate the effects of backbone architecture and training objective, we standardize all other implementation choices across baselines.

Shared I/O and head. All models use the same heterogeneous graph schema (Section 2.4) and a shared output head that maps final node embeddings to predicted ACOF variables, including identical normalization and clipping for box constraints.

Matched training budgets. We train all backbones under the same samples-seen budget and early-stopping logic, and we apply the same two-stage HPO protocol with a matched number of trials per model family (Section 4.1).

Optimization and regularization. We use the same optimizer family (AdamW), gradient clipping, and dropout conventions across models; only architecture-specific hyperparameters (e.g., number of layers, hidden dimension, attention heads) vary within the HPO search space.

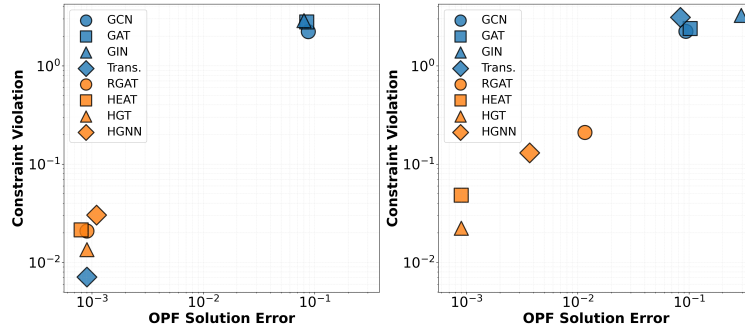
Metric reporting. We report the same accuracy and feasibility metrics for all models (Section 2.5), using fixed dataset splits and consistent aggregation over random seeds.

5 Benchmark Results and Analysis

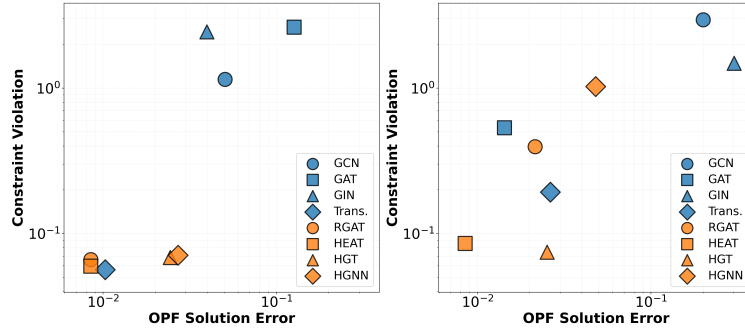
This section reports benchmark results across tasks and distills empirical findings on how architecture, training regime (single vs. multi-topology), and constraint-aware objectives affect accuracy, feasibility, and transfer behavior.

5.1 Single- and Multi-Topology Baselines

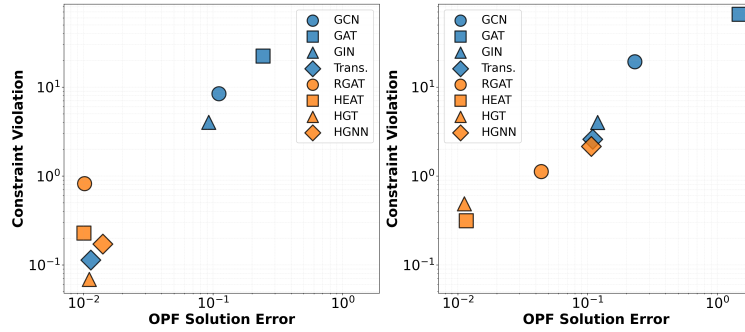
Figure 1 shows a consistent architecture ranking across all three test topologies. With single-topology training (left panels), heterogeneous models cluster in the lower-left region, achieving both lower solution error and smaller violations; among homogeneous baselines, transformer is the only one that remains competitive, while GCN/GAT/GIN show significantly higher errors and violations. With multi-topology training (right panels), heterogeneous models largely retain their advantage with only modest degradation, whereas homogeneous models deteriorate more noticeable in both accuracy and feasibility. HGT and HEAT are the most robust across both regimes. Violations increase under multi-topology training, particularly evident on case118, consistent with reduced per-topology samples in joint training, but remain within acceptable bounds for heterogeneous models, indicating effective cross-topology knowledge transfer. As network size grows, both prediction error and constraint violations increase, with feasibility degradation more pronounced on larger cases, especially under multi-topology training. Detailed results are provided in Appendix E.



(a) Evaluation on case30



(b) Evaluation on case57



(c) Evaluation on case118

Figure 1: Architecture comparison on single-topology (left) vs. multi-topology (right) training. Heterogeneous architectures generally demonstrate better performances than homogeneous models in both solution quality and constraint satisfaction, especially in multi-topology training.

5.2 Comparison of Graph Architectures

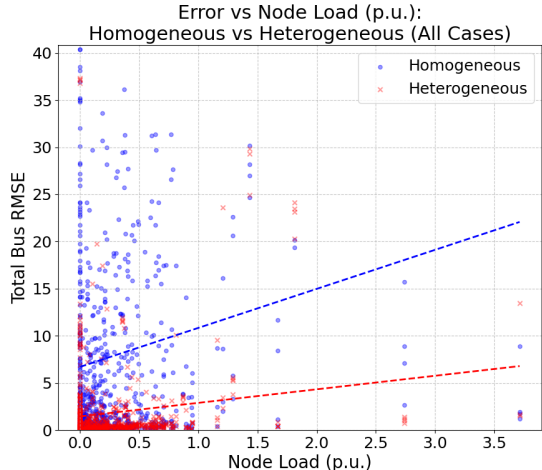


Figure 2: Model error on held-out test data across cases 14, 30, 57,118, 500, 2000 with respect to total system load across homogeneous and heterogeneous categories. Higher system load is generally correlated with error, but heterogeneous models generalize to unseen high-load cases significantly better than homogeneous ones.

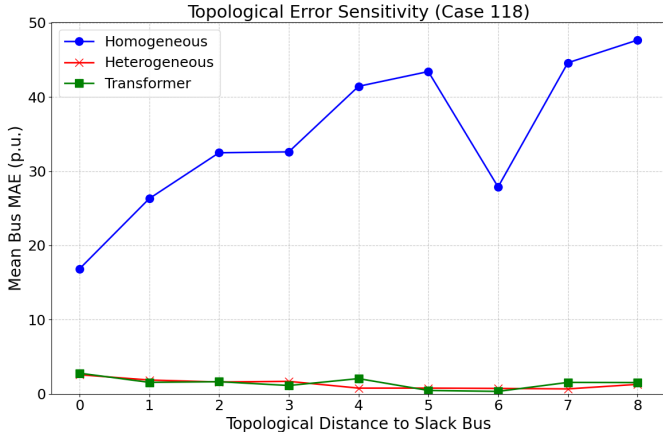
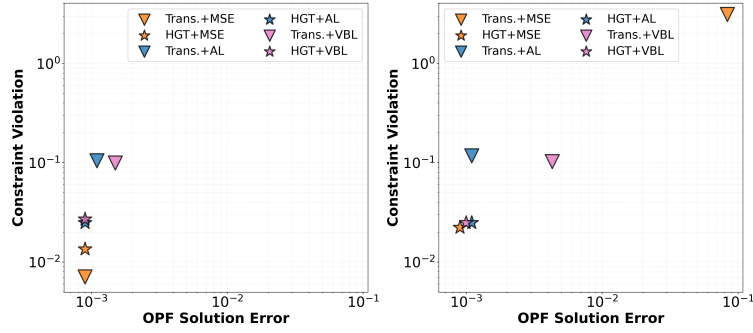


Figure 3: MAE contribution of individual buses with respect to their topological distance to reference (i.e. how many jumps there are between a given bus and a slack bus). Transformers perform significantly differently from other homogeneous models (average performance of GAT, GCN, GIN shown), with model accuracy being unaffected by distance to reference.

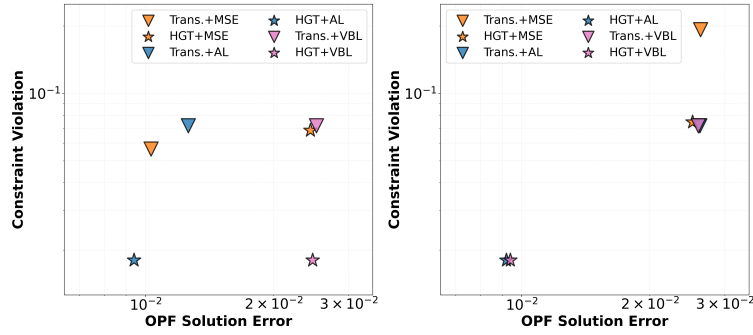
Across cases and training regimes, heterogeneous GNNs (HGT, HEAT, RGAT, HGNN) yield the most consistent accuracy–feasibility trade-offs, the most apparent under multi-topology training and topology shift. In contrast, homogeneous message-passing baselines (GCN/GAT/GIN) degrade more sharply as operating conditions shift, with noticeably weaker generalization to high load regimes (Figure 2) and larger errors as topological distance increases (Figure 3). Among homogeneous models, the graph Transformer is the only architecture that consistently approaches heterogeneous performance, and exhibits near-zero dependence of error on topological distance, suggesting stronger global generalization; see Figure 3. We provide representational evidence via intermediate-layer PCA and linear probing analyses in Appendix F.

5.3 Effect of Loss Function Design

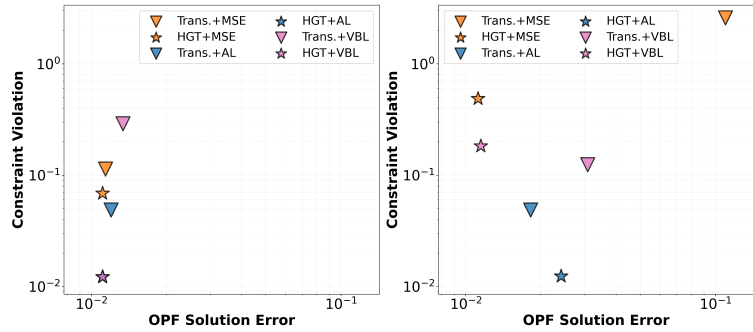
Figure 4 demonstrates the joint importance of architecture and loss function selection. Transformer with MSE excels on small single-topology tasks, especially on the OPF solution predictions, but degrades significantly



(a) Evaluation on case30



(b) Evaluation on case57



(c) Evaluation on case118

Figure 4: Loss function comparison across architectures under equal training budgets. Left panels: single-topology training. Right panels: multi-topology training on cases 30, 57 and 118. Each architecture evaluated with three loss functions (MSE, AL, VBL).

with scale where violations increase an order of magnitude from case30 to case118 under single-topology training and struggles under multi-topology training. This implies that Transformer performs effective representation learning on label prediction, especially in small power grid topologies. HGT with AL exhibits opposite behavior. This combination shows very consistent performance across all configurations. Its superior performances are obvious under multi-topology training compared to other combinations. Notably, HGT, regardless of loss function choices, maintains lower prediction error. In general, we observe MSE produces highest violations compared to AL and VBL, while VBL offers slightly worse constraint violation controls than AL. These results demonstrate that AL loss effectively guides the training to satisfy physical constraints while minimizing the label prediction error and scales well into large-scale power grid topologies.

To evaluate the changes loss choice induces in the model’s internal representation of the problem, we use linear probes [1] to approximate a notion of how linearly classifiable different physical grid characteristics are across progressively deeper layers of a model. Two facts stand out. First, the model’s representation of system characteristics becomes increasingly nonlinear with AL compared to MSE without impacting loss, pointing to the idea that AL is inducing a greater degree of physics structure in the model. The same model and layer with the use of AL loss induce markedly different structure in the activations for the same data. This additional degree of structure brought on by a more physics-aware loss may account in part for the improved generalization performance to unseen cases.

Adding an explicit cost objective induces a systematic shift in the feasibility–optimality tradeoff rather than a uniform improvement along a single axis, as shown in Figure 5. Without the cost term, solutions concentrate at lower violation norms while exhibiting higher and more dispersed generation costs, yet remain within a 0.1% optimality gap of the ground-truth solution cost due to supervision on cost-optimal ACOPF solutions. Incorporating the cost objective further reduces generation cost but does so at the expense of increased constraint violation, reflected by a clear displacement of the solution centroid along the Pareto frontier in cost–violation space. This behavior indicates that, in the supervised setting, the model already internalizes cost structure through solution-level supervision, and that explicitly optimizing cost provides limited additional benefit while biasing training away from feasibility.

Additional representational diagnostics comparing AL vs. MSE training are provided in Appendix F.

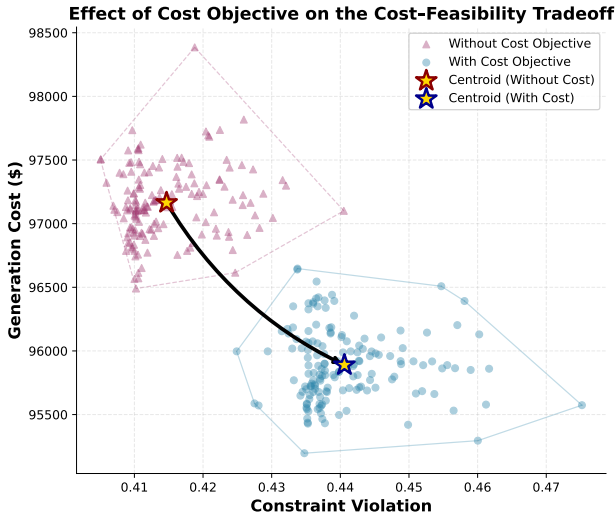


Figure 5: Cost–feasibility tradeoff with and without cost objective

5.4 Scaling Behavior Across Network Sizes

Figure 6 shows the topology-normalized constraint violation as a function of grid size under a fixed budget of 1M test samples per topology for training Transformer with MSE loss function. Violations remain near zero for small and medium networks (case30 to case57), increasing from ≈ 0.06 to ≈ 0.17 , indicating effective constraint control in this regime. A clear transition occurs at case118, where violations rise to ≈ 0.69 , followed by a sharp increase at case500 (≈ 15.4). A power-law fit across cases suggests superlinear scaling

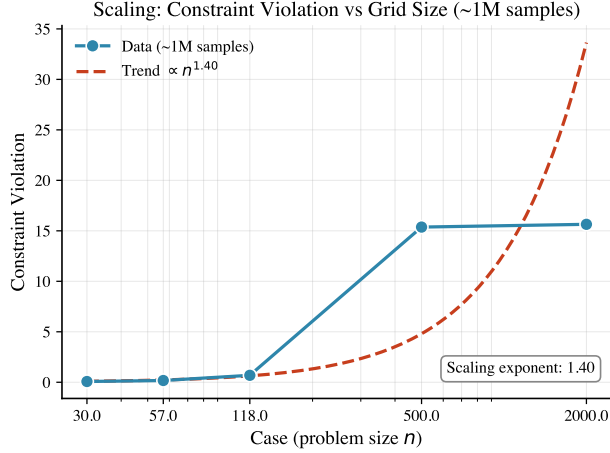


Figure 6: Topology-normalized total constraint violation across increasing power-grid sizes. Results are evaluated on a fixed budget of 1M test samples per case. The dashed curve illustrates an empirical scaling trend.

with an empirical exponent of ≈ 1.40 . However, violations saturate between case500 and case2000 (≈ 15.6), indicating that feasibility degradation does not increase monotonically with network size at extreme scales. The fitted exponent therefore reflects an empirical scaling trend over small-to-large systems rather than a universal law.

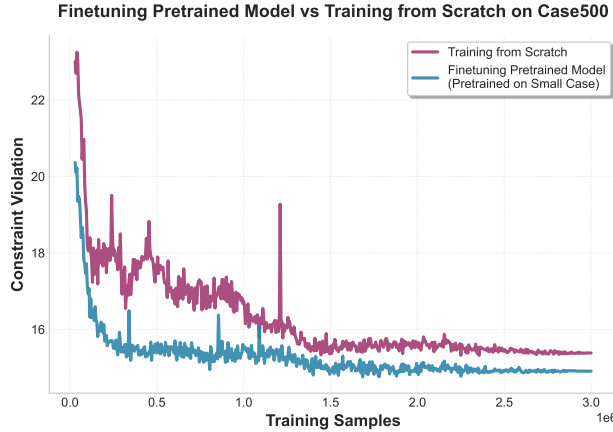


Figure 7: Constraint violation convergence on case500: fine-tuning vs. training from scratch

5.5 Generalization Across Power System Topologies

Finetuning vs. Training from Scratch. Figure 7 and Table 1 jointly demonstrate that pretraining primarily improves convergence speed while also contributing to lower final violation on large topologies. On case-500, fine-tuning from a small-case pretrained model reaches the same violation threshold (i.e., 15.5) achieved by training from scratch at 1.3M samples using only 215K training steps, corresponding to an 83.6% reduction in optimization steps. This accelerated convergence is evident in Figure 7, where the fine-tuned model rapidly suppresses large initial violations and stabilizes early, while training from scratch exhibits prolonged high-variance dynamics and slower decay. In addition, fine-tuning achieves a 3.1% reduction in the final violation norm on case-500, indicating that pretraining not only reduces the sample complexity required to reach a given feasibility level but also yields improved feasibility. For the smaller case-118, fine-tuning yields both faster convergence (48.8% fewer steps) and a larger improvement in final violation (25.1%),

suggesting that representation transfer is more effective when the target topology is closer in scale to the pretraining regime. Overall, these results indicate that foundation-style pretraining amortizes optimization effort across topologies by initializing models in a low-violation basin, yielding order-of-magnitude reductions in training steps on large grids while consistently improving final feasibility.

Table 1: Convergence comparison between training from scratch and fine-tuning across grid sizes. Improvements in final violation and training steps are shown as blue subscripts.

Case	Total Violation Norm		Training Steps	
	Scratch	Finetuned	Scratch	Finetuned
118	8.986	6.732 _(-25.1%)	3,000,000	1,535,008 _(-48.8%)
500	15.387	14.910 _(-3.1%)	1,310,048	215,008 _(-83.6%)

Zero-Shot Transfer to Unseen Topologies. We select Transformer and HGT for zero-shot transfer evaluation as they demonstrate advantages over other architectures in prior experiments, with Transformer with MSE and HGT with AL emerging as best-in-class models. We additionally evaluate HGT with MSE to isolate the effect of architecture from loss function, given MSE’s simplicity. Table 2 presents the results across these configurations. Single-topology transfer (rows 1-2) demonstrates a clear solution quality-feasibility trade-off: Transformer with MSE achieves the lowest OPF solution error when transferring from case30 to larger networks but produces substantially higher constraint violations, while HGT with AL loss maintains significantly lower constraint violations at comparable solution qualities. In Multi-topology training (rows 3-5), HGT demonstrates superior transfer robustness to Transformer, achieving consistently smaller constraint violations compared to Transformer with the same MSE loss function. Comparing loss functions, AL reduces violations by an order of magnitude relative to MSE across all transfer scenarios, establishing constraint-aware training as essential for foundation model training and deployment.

Table 2: Zero-shot transfer and multi-topology pretraining results. Best performance for each training→evaluation scenario shown in bold.

Training → Eval	Trans.+MSE		HGT+MSE		HGT+AL	
	OPF Sol. Err.	Viol.	OPF Sol. Err.	Viol.	OPF Sol. Err.	Viol.
case30 → case57	4.743	5.053	5.299	2.060	5.311	0.230
case30 → case118	1.912	9.118	2.030	3.766	2.030	1.262
case{57,118} → case30	1.120	4.853	0.4693	2.286	0.547	0.239
case{30,118} → case57	5.677	1.990	5.6337	1.4781	5.225	0.018
case{30,57} → case118	2.011	26.295	6.173	12.26	2.837	0.907

5.6 Sensitivity to Numerical Precision

Mixed-precision training with BF16 consistently accelerates optimization across network sizes, with gains increasing as problem scale grows (Figure 8). On case118, training time decreases from 52 to 32 minutes (38.5%), while on case500 it decreases from 134 to 79 minutes (41.0%), with absolute training timesavings rising from 20 to 55 minutes. This scaling behavior indicates that BF16 primarily reduces the dominant compute and memory costs associated with large graph message passing and constraint-aware loss evaluation, rather than providing a fixed-factor speedup. In contrast, FP32 training exhibits steeper runtime growth with case size, whereas BF16 moderates this scaling, improving effective hardware utilization on large instances. These results show that mixed precision is especially beneficial in large-grid and multi-topology training regimes central to foundation-style OPF surrogates, enabling substantial reductions in training cost without altering model structure or feasibility-aware objectives.

5.7 Failure Modes and Diagnostics

Finally, we identify topological complexity as a crucial factor that may limit the performances of foundation-style pretraining from our analyses of failure cases. Node-level error correlates with node degree ($r = 0.51$)

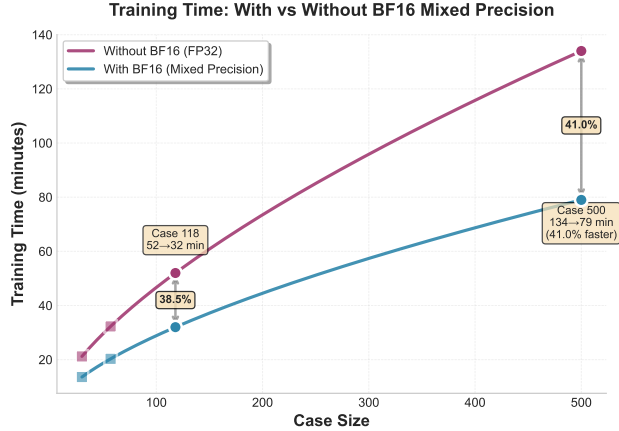


Figure 8: Training time vs. case size with and without mixed precision training(BF16)

irrespective of model type. This suggests that although we see good generalization across cases, model error tends to be concentrated around topologically complex grid regions as shown in Figure 9. This diagnostic provides guidance for future dataset expansion and model improvements, and highlights the importance of combining foundation models with domain-specific safety checks in operational settings.

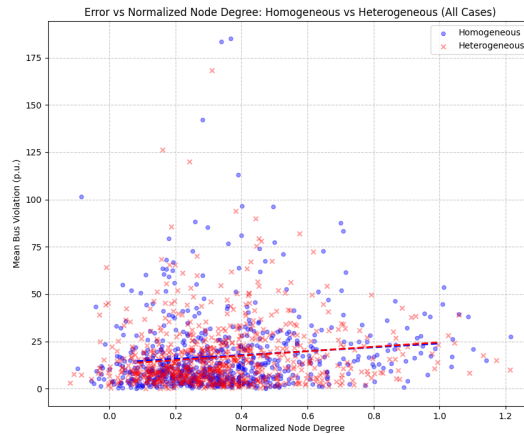


Figure 9: Model error across categories with respect to node degree, across cases 14, 30, 57, 118, 500, 2000 with degree normalized with respect to case maximum degree. Model error by node correlates with node degree ($r = 0.51$).

6 Conclusion

This work introduced a comprehensive benchmarking suite for evaluating surrogate model performance for AC optimal power flow, along with a systematic study comparing a range of different homogeneous and heterogeneous graph neural network architectures under three constraint-aware objectives. Our experiments yield several insights for the broader research community.

Firstly, architecture matters and models capable of exploiting graph heterogeneity significantly outperform homogeneous variants, with HGT achieving the best overall performance. Among homogeneous models, models perform well if they are able to learn implicit encodings of node types or capture global dependencies between nodes (as in the Transformer case), making it clear that choices around the underlying graph representation have a significant impact on model training.

Secondly, embedding constraint-awareness in the choice of loss is critical to model generalization. Using MSE as a target yields higher violations under distribution shift, with AL and VBL loss providing increasing

performance improvements. Generalization performance depends primarily on the constraint-awareness of the loss and the training regime, with multi-topology pretraining having a significant impact on generalization to unseen grids particularly with an AL loss. Overall we find HGT with constraint-aware losses to be a promising approach for zero-shot transfer.

There are some limitations to this analysis however. As is the case with many approaches to ACOPF problems, lack of data availability from real grids requires us to train on synthetic data. This increases the relevance of common benchmarks and benchmarking tools to the broader research community. However, even though several of the topologies selected are standard IEEE test systems and others are generated using real grid statistics[3], there may be physical grid conditions not captured by the synthetic data. This may limit generalization to real-world scenarios without fine-tuning, although we demonstrate that multi-topology pretraining may effectively limit the amount of fine-tuning data required.

As grid modernization continues to increase operational complexity, fast and reliable ACOPF surrogates will be critical for operators to strengthen the resilience of the grid, and this suite contributes a standardized set of research benchmarks and models in support of that aim.

Acknowledgments

This material is based upon work supported by Laboratory Directed Research and Development (LDRD) funding from Argonne National Laboratory, provided by the Director, Office of Science, of the U.S. Department of Energy under contract DE-AC02-06CH11357.

An award of computer time was provided by the ASCR Leadership Computing Challenge (ALCC) program. This research used resources of the Argonne Leadership Computing Facility, which is a U.S. Department of Energy Office of Science User Facility operated under contract DE-AC02-06CH11357.

This research used resources of the National Energy Research Scientific Computing Center (NERSC), a Department of Energy User Facility using NERSC award ALCC-ERCAP0038201.

References

- [1] Guillaume Alain and Yoshua Bengio. Understanding intermediate layers using linear classifier probes. *arXiv preprint arXiv:1610.01644*, 2016.
- [2] Daniel Bienstock and Abhinav Verma. Strong np-hardness of ac power flows feasibility. *Operations Research Letters*, 47(6):494–501, 2019.
- [3] Adam B Birchfield, Ti Xu, Kathleen M Gegner, Komal S Shetye, and Thomas J Overbye. Grid structural characteristics as validation criteria for synthetic networks. *IEEE Transactions on power systems*, 32(4):3258–3265, 2016.
- [4] Sarra Bouchkati, Philipp Lutat, Luis Böttcher, Florian Klein-Helmkamp, and Andreas Ulbig. Augmented lagrangian guided learning for the optimal power flow problem. *IFAC-PapersOnLine*, 58(13):50–55, 2024.
- [5] Dan Busbridge, Dane Sherburn, Pietro Cavallo, and Nils Y. Hammerla. Relational graph attention networks, 2019.
- [6] J. Carpentier. Contribution à l’étude du dispatching économique. *Bulletin de la Société Française des Électriciens*, 3(8):431–447, 1962.
- [7] Kejun Chen, Shourya Bose, and Yu Zhang. Physics-informed gradient estimation for accelerating deep learning-based ac-opf. *IEEE Transactions on Industrial Informatics*, 2025.
- [8] Amir Deihim, Despina Apostolopoulou, and Eduardo Alonso. Initial estimate of AC optimal power flow with graph neural networks. *Electric Power Systems Research*, 234:110782, 2024.

- [9] Ferdinando Fioretto, Terrence WK Mak, and Pascal Van Hentenryck. Predicting AC optimal power flows: Combining deep learning and lagrangian dual methods. In *Proceedings of the AAAI conference on artificial intelligence*, volume 34, pages 630–637, 2020.
- [10] Stephen Frank, Ingrida Steponavice, and Steffen Rebennack. Optimal power flow: A bibliographic survey i: Formulations and deterministic methods. *Energy systems*, 3(3):221–258, 2012.
- [11] Stephen Frank, Ingrida Steponavice, and Steffen Rebennack. Optimal power flow: A bibliographic survey ii: Non-deterministic and hybrid methods. *Energy systems*, 3(3):259–289, 2012.
- [12] Maosheng Gao, Juan Yu, Zhifang Yang, and Junbo Zhao. A physics-guided graph convolution neural network for optimal power flow. *IEEE Transactions on Power Systems*, 39(1):380–390, 2023.
- [13] Hendrik F Hamann, Blazhe Gjorgiev, Thomas Brunschwiler, Leonardo SA Martins, Alban Puech, Anna Varbella, Jonas Weiss, Juan Bernabe-Moreno, Alexandre Blondin Massé, Seong Lok Choi, et al. Foundation models for the electric power grid. *Joule*, 8(12):3245–3258, 2024.
- [14] Doan Thanh Hien, Keunju Song, Kibaek Kim, and Hongseok Kim. Alternative learning architecture for solving ac-opf via supervised relaxation and cross encoder. In *NeurIPS Workshop on GPU-Accelerated and Scalable Optimization*, 2025.
- [15] Ziniu Hu, Yuxiao Dong, Kuansan Wang, and Yizhou Sun. Heterogeneous graph transformer. In *Proceedings of the web conference 2020*, pages 2704–2710, 2020.
- [16] Wanjun Huang, Xiang Pan, Minghua Chen, and Steven H. Low. DeepOPF-V: Solving AC-OPF problems efficiently. *IEEE Transactions on Power Systems*, 37(1):800–803, 2022.
- [17] Youngdae Kim and Kibaek Kim. Accelerated computation and tracking of ac optimal power flow solutions using gpus. In *Workshop Proceedings of the 51st International Conference on Parallel Processing*, pages 1–8, 2022.
- [18] TN Kipf. Semi-supervised classification with graph convolutional networks. *arXiv preprint arXiv:1609.02907*, 2016.
- [19] Bowen Li and Kibaek Kim. Gpu-accelerated sequential quadratic programming algorithm for solving acopf. In *2024 IEEE 63rd Conference on Decision and Control (CDC)*, 2024.
- [20] Shaohui Liu, Chengyang Wu, and Hao Zhu. Topology-aware graph neural networks for learning feasible and adaptive ac-opf solutions. *IEEE Transactions on Power Systems*, 38(6):5660–5670, 2022.
- [21] Sean Lovett, Miha Zgubic, Sofia Liguori, Sephora Madjiheurem, Hamish Tomlinson, Sophie Elster, Chris Apps, Sims Witherspoon, and Luis Piloto. Opfdata: Large-scale datasets for ac optimal power flow with topological perturbations. *arXiv preprint arXiv:2406.07234*, 2024.
- [22] Xiaoyu Mo, Zhuyu Huang, Yang Xing, and Chen Lv. Multi-agent trajectory prediction with heterogeneous edge-enhanced graph attention network. *IEEE Transactions on Intelligent Transportation Systems*, 23(7):9554–9567, 2022.
- [23] J.A. Momoh, R. Adapa, and M.E. El-Hawary. A review of selected optimal power flow literature to 1993. i. nonlinear and quadratic programming approaches. *IEEE Transactions on Power Systems*, 14(1):96–104, 1999.
- [24] Alexis Montoison, François Pacaud, Michael Saunders, Sungho Shin, and Dominique Orban. Madncl: a gpu implementation of algorithm ncl for large-scale, degenerate nonlinear programs. *arXiv preprint arXiv:2510.05885*, 2025.
- [25] Rahul Nellikkath and Spyros Chatzivasileiadis. Physics-informed neural networks for ac optimal power flow. *Electric Power Systems Research*, 212:108412, 2022.

- [26] Damian Owerko, Fernando Gama, and Alejandro Ribeiro. Optimal power flow using graph neural networks. In *Proc. IEEE International Conference on Acoustics, Speech and Signal Processing (ICASSP)*, pages 5930–5934, Barcelona, Spain, 2020.
- [27] François Pacaud, Armin Nurkanović, Anton Pozharskiy, Alexis Montoison, and Sungho Shin. An augmented lagrangian method on gpu for security-constrained ac optimal power flow. *arXiv preprint arXiv:2510.13333*, 2025.
- [28] Xiang Pan, Minghua Chen, Tianyu Zhao, and Steven H. Low. DeepOPF: A feasibility-optimized deep neural network approach for AC optimal power flow problems. *IEEE Systems Journal*, 17(1):673–683, 2023.
- [29] Xiang Pan, Wanjun Huang, Minghua Chen, and Steven H. Low. DeepOPF-AL: Augmented learning for solving AC-OPF problems with a multi-valued load-solution mapping. In *The 14th ACM International Conference on Future Energy Systems (e-Energy '23)*, pages 391–396, Orlando, FL, USA, 2023.
- [30] Luis Piloto, Sofia Liguori, Sephora Madjiheurem, Miha Zgubic, Sean Lovett, Hamish Tomlinson, Sophie Elster, Chris Apps, and Sims Witherspoon. Canos: A fast and scalable neural ac-opf solver robust to n-1 perturbations. *arXiv preprint arXiv:2403.17660*, 2024.
- [31] Sungho Shin, Mihai Anitescu, and François Pacaud. Accelerating optimal power flow with gpus: Simd abstraction of nonlinear programs and condensed-space interior-point methods. *Electric Power Systems Research*, 236:110651, 2024.
- [32] Sungho Shin, Vishwas Rao, Michel Schanen, D Adrian Maldonado, and Mihai Anitescu. Scalable multi-period ac optimal power flow utilizing gpus with high memory capacities. In *2024 Open Source Modelling and Simulation of Energy Systems (OSMSES)*, pages 1–6. IEEE, 2024.
- [33] Petar Veličković, Guillem Cucurull, Arantxa Casanova, Adriana Romero, Pietro Lio, and Yoshua Bengio. Graph attention networks. *arXiv preprint arXiv:1710.10903*, 2017.
- [34] Junfei Wang and Pirathayini Srikantha. Data-driven ac optimal power flow with physics-informed learning and calibrations, 2024.
- [35] Keyulu Xu, Weihua Hu, Jure Leskovec, and Stefanie Jegelka. How powerful are graph neural networks? *arXiv preprint arXiv:1810.00826*, 2018.
- [36] Mei Yang, Gao Qiu, Junyong Liu, Youbo Liu, Tingjian Liu, Zhiyuan Tang, Lijie Ding, Yue Shui, and Kai Liu. Topology-transferable physics-guided graph neural network for real-time optimal power flow. *IEEE Transactions on Industrial Informatics*, 20(9):10857–10872, 2024.
- [37] Seongjun Yun, Minbyul Jeong, Raehyun Kim, Jaewoo Kang, and Hyunwoo J Kim. Graph transformer networks. *Advances in neural information processing systems*, 32, 2019.
- [38] Sihan Zeng, Youngdae Kim, Yuxuan Ren, and Kibaek Kim. Qcqp-net: Reliably learning feasible alternating current optimal power flow solutions under constraints. In *6th Annual Learning for Dynamics & Control Conference*, volume 242, 2024.
- [39] Chuxu Zhang, Dongjin Song, Chao Huang, Ananthram Swami, and Nitesh V. Chawla. Heterogeneous graph neural network. In *Proceedings of the 25th ACM SIGKDD International Conference on Knowledge Discovery & Data Mining (KDD)*, pages 793–803, 2019.

The submitted manuscript has been created by UChicago Argonne, LLC, Operator of Argonne National Laboratory (“Argonne”). Argonne, a U.S. Department of Energy Office of Science laboratory, is operated under Contract No. DE-AC02-06CH11357. The U.S. Government retains for itself, and others acting on its behalf, a paid-up nonexclusive, irrevocable worldwide license in said article to reproduce, prepare derivative works, distribute copies to the public, and perform publicly and display publicly, by or on behalf of the Government. The Department of Energy will provide public access to these results of federally sponsored research in accordance with the DOE Public Access Plan

A AC Branch-flow Formulation

The active and reactive power flows (from i to j) are defined as

$$P_{ij}(V, \theta) := V_i^2 G_{ij} - V_i V_j (G_{ij} \cos(\theta_{ij}) + B_{ij} \sin(\theta_{ij})), \quad (6)$$

$$Q_{ij}(V, \theta) := -V_i^2 B_{ij} - V_i V_j (G_{ij} \sin(\theta_{ij}) - B_{ij} \cos(\theta_{ij})), \quad (7)$$

where $P_{d,i}$, $Q_{d,i}$ are the active and reactive loads for bus $i \in \mathcal{N}$, V_i , θ_i are the voltage magnitude and angle, $\theta_{ij} = \theta_i - \theta_j$, and $Y_{ij} = G_{ij} + jB_{ij}$ is the element of the bus admittance matrix.

B Full Node/Edge Features in Graph Representation

Nodes and edges correspond to physical components of the grid. The node set \mathcal{V} comprises four node types:

- *Buses*: voltage bounds (V_i^{min}, V_i^{max}) and a one-hot bus type (PQ/PV/slack).
- *Generators*: ($P_g^{min}, P_g^{max}, Q_g^{min}, Q_g^{max}$) and cost coefficients.
- *Loads*: ($P_{d,i}, Q_{d,i}$).
- *Shunts*: (G_s, B_s).

Edges \mathcal{E} correspond to transmission lines and transformers, representing connectivity between buses. Edge features include line parameters derived from the admittance matrix Y_{ij} and thermal limits S_{ij}^{max} .

C Baseline Model Update Equations

C.1 Homogeneous Models.

Homogeneous GNNs use a shared set of parameters across all nodes and edges, and do not explicitly condition their message functions on node or edge types.

GCN: Graph convolutional networks [18] perform normalized neighborhood aggregation. Using self-loops and $\tilde{A} = A + I$, $\tilde{D}_{ii} = \sum_j \tilde{A}_{ij}$, the layer update can be written as

$$h_i^{\ell+1} = \sigma \left(W^\ell \sum_{i,j \in \mathcal{N}(i)} \frac{1}{\sqrt{d_i d_j}} h_j^\ell \right).$$

Note that GCNs only capture adjacency, ignoring edge features entirely.

GAT: Graph attention networks [33] learn attention weights over neighbors. For a single head,

$$\alpha_{ij}^\ell = \text{softmax}(\text{LeakyReLU}(a[Wh_i^\ell || Wh_j^\ell])),$$

with layer updates given by:

$$h_i^{\ell+1} = \sigma \left(\sum_{j \in \mathcal{N}} \alpha_{ij}^\ell W h_j^\ell \right).$$

GIN: Graph Isomorphism networks [35] use an MLP after aggregating node features over a neighborhood like:

$$h_i^\ell = \text{MLP}^\ell \left((1 + \epsilon^\ell) h_i^\ell + \sum_{j \in \mathcal{N}(i)} h_j^\ell \right).$$

Graph Transformer: Graph transformers [37] do not explicitly encode node or edge type information, but do have global attention, which may give a model a way to capture global node-node relationships that

would otherwise be captured explicitly by node type. As in [37] we model the query/key/value tuple for a given layer like:

$$Q^{(\ell)} = H^{(\ell)}W_Q^{(\ell)}, \quad K^{(\ell)} = H^{(\ell)}W_K^{(\ell)}, \quad V^{(\ell)} = H^{(\ell)}W_V^{(\ell)},$$

where $H^{(\ell)} \in \mathbb{R}^{|\mathcal{V}| \times d_\ell}$ stacks node embeddings. Attention is then computed as

$$\text{Attn}(Q, K, V) = \text{softmax}\left(\frac{QK^\top}{\sqrt{d_k}} + M\right)V,$$

where M is an attention mask encoding adjacency-restricted attention.

C.2 Heterogeneous Models.

Fully heterogeneous GNNs encode both node types t_i and edge types r_{ij} , using type-specific transformations. This is well-matched to power-grid structure, where buses, generators, loads, and shunts play distinct physical roles and participate in different subsets of constraints.

RGAT: Relational graph attention network [5] attempt to explicitly encode edge relations of different types by giving each edge category its own projection matrices

$$m_{ij}^\ell = W_{r_{ij}}^\ell h_j^\ell, \quad \alpha_{ij}^\ell = \text{softmax}(\text{score}(h_i^\ell, h_j^\ell, r(i, j), e_{ij}))$$

where layer updates are then given by

$$h_i^\ell = \sigma\left(\sum_{j \in \mathcal{N}} (\alpha_{ij}^\ell m_{ij}^\ell)\right).$$

HeteroGNN: Heterogeneous graph neural networks [39], are a straightforward extension of GNNs that learn a feature projection for each node type and aggregate messages from node-type specific neighborhoods. Layer updates are given by:

$$h_i^{\ell+1} = \sigma(W_t^\ell h_i^\ell + \sum_{\tau \in \mathcal{T}} \text{AGG}(h_\tau^\ell))$$

where $\tau \in \mathcal{T}$ is a typed node from a neighborhood of adjacent nodes of that type.

HGT: Heterogeneous Graph Transformer (HGT) [15] combines typed message passing with multi-head attention. For node i attending to neighbor j along edge relation r_{ij} with node types t_i, t_j , HGT uses type-dependent projections giving Q/K/V like:

$$q_i^{(\ell)} = W_Q^{(\ell, t_i)} h_i^{(\ell)}, \quad k_j^{(\ell)} = W_K^{(\ell, t_j)} h_j^{(\ell)}, \quad v_j^{(\ell)} = W_V^{(\ell, t_j)} h_j^{(\ell)}$$

An attention model that attends to type-specific connections like:

$$s_{ij}^\ell = \frac{\left(q_i^{(\ell)}\right)^\top \left(W_A^{(\ell, r_{ij})} k_j^{(\ell)}\right)}{\sqrt{d_k}}, \quad \alpha_{ij}^{(\ell)} = \text{softmax}_{j \in \mathcal{N}(i)}(s_{ij}^\ell).$$

HEAT: Heterogeneous edge attention transformers [22] are a category of transformer that augments typed attention with additional edge-enhancement. HEAT follows the same typed message passing template as above, with attention scores and messages explicitly conditioned on $(t_i, t_j, r_{ij}, e_{ij})$:

$$m_{ij}^{(\ell)} = \phi^{(\ell)}\left(h_i^{(\ell)}, h_j^{(\ell)}, e_{ij}, t_i, t_j, r_{ij}\right), \quad h_i^{(\ell+1)} = \sigma\left(\sum_{j \in \mathcal{N}(i)} \alpha_{ij}^{(\ell)} m_{ij}^{(\ell)}\right),$$

where $\phi^{(\ell)}(\cdot)$ is a learnable message function and $\alpha_{ij}^{(\ell)}$ is computed by a typed attention mechanism.

D Hyperparameter Configurations

D.1 Hyperparameter optimization settings.

Tables 3 and 4 detail the hyperparameter ranges and sampling strategies for Stage 1 (architecture and learning sweep) and Stage 2 (loss function sweep), respectively.

Table 3: Stage 1 Hyperparameter Ranges for Architecture Sweep (50 configurations per architecture)

Architecture	Hyperparameters and Ranges
GAT, GCN, GIN, Transformer, HGNN	Number of layers: [3, 4, 6] Hidden dimensions: [128, 256, 512] Dropout: [0.0, 0.3], uniform Learning rate: $[1 \times 10^{-4}, 3 \times 10^{-3}]$, log-uniform Weight decay: $[1 \times 10^{-6}, 1 \times 10^{-2}]$, log-uniform Gradient clip value: [0.5, 2.0], uniform
HEAT	Number of layers: [3, 4, 6] Hidden dimensions: [128, 256, 512] Dropout: [0.0, 0.3], uniform Number of attention heads: [2, 4, 8] Learning rate: $[1 \times 10^{-4}, 3 \times 10^{-3}]$, log-uniform Weight decay: $[1 \times 10^{-6}, 1 \times 10^{-2}]$, log-uniform Gradient clip value: [0.5, 2.0], uniform
HGT	Number of layers: [3, 4, 6] Hidden dimensions: [128, 256, 512] Dropout: [0.0, 0.3], uniform Number of heads: [2, 4, 8] Learning rate: $[1 \times 10^{-4}, 3 \times 10^{-3}]$, log-uniform Weight decay: $[1 \times 10^{-6}, 1 \times 10^{-2}]$, log-uniform Gradient clip value: [0.5, 2.0], uniform
RGAT	Number of layers: [3, 4, 6] Hidden dimensions: [128, 256, 512] Dropout: [0.0, 0.3], uniform Number of heads: [2, 4, 8] Edge dim: [2, 4, 8] Learning rate: $[1 \times 10^{-4}, 3 \times 10^{-3}]$, log-uniform Weight decay: $[1 \times 10^{-6}, 1 \times 10^{-2}]$, log-uniform Gradient clip value: [0.5, 2.0], uniform

D.2 Hyperparameter sensitivity and robustness.

Figure 10 show training progression for nine representative configurations grouped by performance selected from stable runs. The first two plots compare stage 1 sweep with Transformer and HGT trained with MSE loss function. The Transformer architecture converges rapidly within the first 500K samples, but exhibits a wide performance spread in OPF solution error. The constraint violations decrease more gradually with best configurations. HGT shows tighter clustering compared to Transformer and achieves superior constraint satisfaction in top configurations. In stage 2 sweep, we compare AL and VBL loss functions on HGT. Both exhibit high sensitivity to hyperparameters with substantial performance variance. AL’s best configuration achieves consistently better constraint violation compared to worse configurations. VBL, however, shows a much noisier convergence. The performance clustering differences between architectures and high loss function sensitivity highlight the critical importance of comprehensive HPO for constrained optimization problems.

E Additional Results

E.1 Single- and Multi-Topology Baselines.

Tables 5-7 compare single-topology and multi-topology pretraining performance across all eight architectures using MSE loss. Each table reports OPF solution errors (OPF Sol. Err.), constraint violations (Viol.), and cost difference (Cost Diff.) for held-out test samples from the evaluated topology. Cost difference quantifies the actual and percentage deviation between generation costs computed from predicted power generation

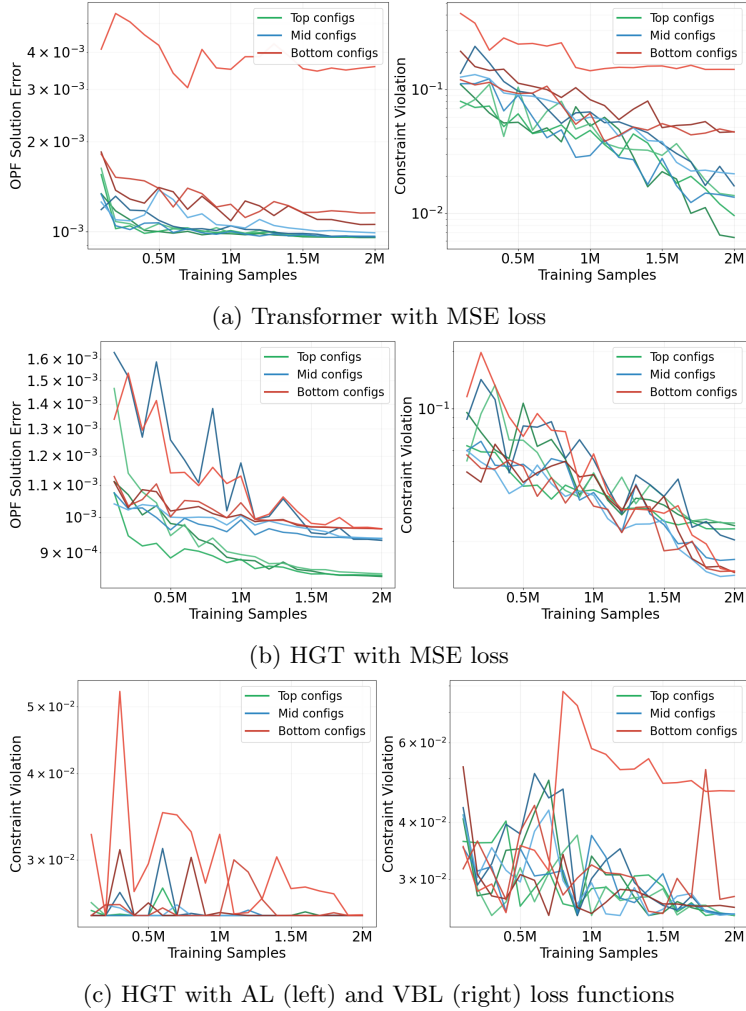


Figure 10: Hyperparameter optimization sensitivity analysis across 2M training samples. (a) Transformer with MSE loss exhibits high performance spread in OPF solution error with rapid early convergence. (b) HGT with MSE loss demonstrates tighter performance clustering and superior constraint satisfaction. (c) HGT loss function comparison reveals high sensitivity to hyperparameters in both AL and VBL methods, with comparable best-case performance.

Table 4: Stage 2 Hyperparameter Ranges for Loss Function Sweep (40 configurations per loss function)

Loss Function	Hyperparameters and Ranges
Augmented Lagrangian (AL), Violation-Based Lagrangian (VBL)	Step size for Lagrangian multipliers update: $[1 \times 10^{-5}, 1 \times 10^{-1}]$, uniform Exponential moving average factor: $[0.0, 1.0]$: uniform Warm-up samples: $[250K, 500K, 750K, 1M, 1.25M, 1.5M]$ Penalty check samples: $[250K, 500K, 750K, 1M, 1.25M, 1.5M]$ Multiplier check samples: $[250K, 500K, 750K, 1M, 1.25M, 1.5M]$

and ground truth optimal power generation, providing an economic measure of solution quality.

Table 5: Evaluation on case30 from single- and multi-topology training with MSE loss function.

Trained on Arch.	Single (case30)			Multi (30+57+118)		
	OPF Sol. Err.	Viol.	Cost Diff.	OPF Sol. Err.	Viol.	Cost Diff.
GCN	0.0876	2.231	-583.65(-35.91%)	0.0934	2.239	-591.29(-36.38%)
GAT	0.0849	2.790	-571.59(-35.17%)	0.1023	2.3976	-506.08(-31.14%)
GIN	0.0801	2.885	-371.65(-22.87%)	0.2936	3.262	1029.97(63.37%)
Trans.	0.0009	0.0071	-0.08(-0.01%)	0.0836	3.114	-184.36(-11.34%)
RGAT	0.0009	0.0209	-3.14(-0.19%)	0.0116	0.21	415.07(25.5%)
HEAT	0.0008	0.0214	-3.08(-0.19%)	0.0009	0.0482	-6.48(-0.40%)
HGT	0.0009	0.0135	-3.19(-0.2%)	0.0009	0.0223	-4.34(-0.27%)
HGNN	0.0011	0.0303	-47.21(-2.9%)	0.0037	0.1303	193.27(11.87%)

Table 6: Evaluation on case57 from single- and multi-topology training with MSE loss function.

Trained on Arch.	Single (case57)			Multi (30+57+118)		
	OPF Sol. Err.	Viol.	Cost Diff.	OPF Sol. Err.	Viol.	Cost Diff.
GCN	0.0505	1.149	-4441.49(-9.13%)	0.200	2.952	-11621.11(-23.89%)
GAT	0.1263	2.620	-7526.33(-15.47%)	0.0143	0.5341	274.15(0.56%)
GIN	0.0397	2.438	-108.03(-0.22%)	0.3018	1.4830	7438.85(15.29%)
Trans.	0.0103	0.0565	-48.16(-0.10%)	0.0263	0.1926	498.63(1.03%)
RGAT	0.0085	0.0662	-48.76(-0.10%)	0.0215	0.3953	3923.45(8.04%)
HEAT	0.0085	0.0596	-44.68(-0.09%)	0.0085	0.0855	-31.5(-0.06%)
HGT	0.0244	0.0684	-136.02(-0.28%)	0.0252	0.0745	-192.29(-0.39%)
HGNN	0.0271	0.0710	-688.55(-1.41%)	0.0480	1.0256	-2934.83(-6.02%)

Table 7: Evaluation on case118 from single- and multi-topology training with MSE loss function.

Trained on Arch.	Single (case118)			Multi (30+57+118)		
	OPF Sol. Err.	Viol.	Cost Diff.	OPF Sol. Err.	Viol.	Cost Diff.
GCN	0.111	8.434	-17806.35(-11.64%)	0.2315	19.308	-2429.87(-1.59%)
GAT	0.243	22.34	-40301.82(-26.33%)	1.477	65.92	-64212.43(-41.96%)
GIN	0.0925	4.013	-7844.08(-5.13%)	0.1197	3.9951	-4695.77(-3.07%)
Trans.	0.0114	0.1136	-224.07(-0.15%)	0.1097	2.5862	-16741.81(-10.94%)
RGAT	0.0102	0.8198	-300.40(-0.20%)	0.0440	1.121	-13787.74(-9.00%)
HEAT	0.0101	0.2278	-292.31(-0.19%)	0.0116	0.3140	-4240.26(-2.77%)
HGT	0.0111	0.0687	-297.97(-0.19%)	0.0112	0.4872	334.86(0.22%)
HGNN	0.0141	0.1718	-2251.08(-1.47%)	0.1070	2.1519	-30316.36(-19.8%)

E.2 Effect of Loss Function Design.

Tables 8-10 compare loss function effects on selected architectures (Transformer and HGT) across three loss functions (MSE, AL, VBL). The same metrics as Tables 5-7 are reported. Models are evaluated on case30, case57, and case118 test sets respectively, with left columns showing single-topology training results and right columns showing multi-topology training (cases 30, 57, and 118) results. Cost difference represents the actual and percentage deviation between generation costs computed from predicted power generation and ground truth optimal power generation.

Table 8: Evaluation on case30 from single- and multi-topology training with selective models and three different loss functions.

Trained on		Single (case30)			Multi (30+57+118)		
Arch.	Loss	OPF Sol. Err.	Viol.	Cost Diff.	OPF Sol. Err.	Viol.	Cost Diff.
GAT	MSE	0.0849	2.790	-571.59(-35.17%)	0.1023	2.3976	-506.08(-31.14%)
	AL	0.1122	0.0995	-394.35(-24.26%)	0.1090	0.1177	-409.07(-25.17%)
	VBL	0.0867	1.9376	-621.35(-38.23%)	0.4245	3.039	247(15.20%)
Trans.	MSE	0.0009	0.0071	-0.08(-0.01%)	0.0836	3.114	-184.36(-11.34%)
	AL	0.0011	0.1048	-0.55(-0.03%)	0.0011	0.1174	41.69(2.57%)
	VBL	0.0015	0.0995	-80.49(-4.95%)	0.0043	0.1026	226.11(13.91%)
HGT	MSE	0.0009	0.0135	-3.19(-0.2%)	0.0009	0.0223	-4.34(-0.27%)
	AL	0.0009	0.0249	-3.39(-0.21%)	0.0011	0.0249	10.11(0.62%)
	VBL	0.0009	0.0270	1.30(0.08%)	0.0010	0.0249	-9.81(-0.6%)

Table 9: Evaluation on case57 from single- and multi-topology training with selective models and three different loss functions.

Trained on		Single (case57)			Multi (30+57+118)		
Arch.	Loss	OPF Sol. Err.	Viol.	Cost Diff.	OPF Sol. Err.	Viol.	Cost Diff.
GAT	MSE	0.1263	2.620	-7526.33(-15.47%)	0.0143	0.5341	274.15(0.56%)
	AL	0.0209	0.0718	-1969.01(-4.05%)	0.0123	0.0718	-661.08(-1.36%)
	VBL	0.2437	2.8357	-11723.59(-24.10%)	0.5510	4.5343	14764.36(30.35%)
Trans.	MSE	0.0103	0.0565	-48.16(-0.10%)	0.0263	0.1926	498.63(1.03%)
	AL	0.0126	0.0718	592.03(1.22%)	0.0262	0.0718	656.70(1.35%)
	VBL	0.0252	0.0718	53.67(0.11%)	0.0260	0.0718	401.57(0.83%)
HGT	MSE	0.0244	0.0684	-136.02(-0.28%)	0.0252	0.0745	-192.29(-0.39%)
	AL	0.0094	0.018	-221.39(-0.45%)	0.0092	0.018	-117.43(-0.24%)
	VBL	0.0247	0.018	-150.33(-0.31%)	0.0094	0.018	186.50(0.38%)

Table 10: Evaluation on case118 from single- and multi-topology training with selective models and three different loss functions.

Trained on		Single (case118)			Multi (30+57+118)		
Arch.	Loss	OPF Sol. Err.	Viol.	Cost Diff.	OPF Sol. Err.	Viol.	Cost Diff.
GAT	MSE	0.243	22.34	-40301.82(-26.33%)	1.477	65.92	-64212.43(-41.96%)
	AL	0.1334	0.0488	-16940.96(-11.07%)	0.1202	0.0531	-11063.21(-7.23%)
	VBL	1.699	66.49	-108897.34(-71.16%)	1.9389	5.5245	-99349.01(-64.92%)
Trans.	MSE	0.0114	0.1136	-224.07(-0.15%)	0.1097	2.5862	-16741.81(-10.94%)
	AL	0.0120	0.0487	656.37 (0.43%)	0.0182	0.0487	-7827.14(-5.11%)
	VBL	0.0134	0.2895	-4901.14(-3.20%)	0.0308	0.1241	-9561.60(-6.25%)
HGT	MSE	0.0111	0.0687	-297.97(-0.19%)	0.0112	0.4872	334.86(0.22%)
	AL	0.0111	0.0122	-297.71(-0.19%)	0.0241	0.0124	-7350.06(-4.80%)
	VBL	0.0111	0.0122	-295.25(-0.19%)	0.0115	0.1824	-850.18(-0.56%)

Figure 11 shows the relative training time for Transformer (left panel) and HGT (right panel) with AL and

VBL loss functions normalized to MSE baseline across different topologies of increasing size. The Transformer exhibits decreasing relative overhead as topology scales, suggesting that complex loss computations become relatively less expensive compared to the attention mechanism. In contrast, HGT maintains consistently low overhead (approximately 10-11%) across all topologies, demonstrating that its sparse message-passing architecture makes loss function complexity nearly negligible regardless of system size.

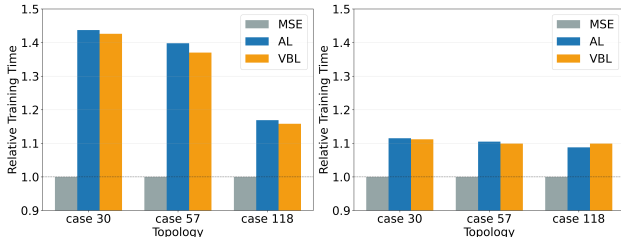


Figure 11: Relative training time for Transformer (left panel) and HGT (right panel) with AL and VBL loss functions normalized to MSE baseline across different topologies.

E.3 Scaling Behavior Across Network Sizes.

To assess model scalability, we train Transformer with MSE loss function on topologies of increasing size (case30 through case2000) using a fixed computational budget of 1M training samples per topology. Table 11 reports performance across five network scales spanning two orders of magnitude (30 to 2000 buses). Despite the fixed sample budget, the model achieves consistently low OPF solution error across all scales (0.001-0.018), demonstrating that solution quality scales well with network complexity, though additional samples would likely further improve performances on larger networks.

Table 11: Performance when scaling across case sizes on 1M samples.

Topology	OPF Sol. Err. ↓	Viol. ↓
case30	0.001146	0.0747
case57	0.018954	0.1744
case118	0.013262	0.6894
case 500	0.006156	15.3711
case 2000	0.007079	15.6446

F Representational Evidence

This appendix provides complementary diagnostic evidence on how different architectures and training objectives shape intermediate representations. We focus on two questions suggested by the main results: (i) whether models without explicit typing (e.g., Transformer) nevertheless learn representations that separate grid component roles, and (ii) whether constraint-aware objectives (AL) change the geometry of learned features relative to pure supervised training (MSE). These analyses are descriptive and are not used for model selection.

F.1 Methodology: PCA visualizations and linear probing

For a trained model, we extract node-level activations $h_i^{(\ell)}$ at selected backbone layers ℓ on held-out samples and perform PCA to visualize dominant directions of variation. Unless otherwise specified, PCA is fit on a random subset of activations and applied to a disjoint subset for visualization. We additionally fit simple linear probes (ridge regression for continuous targets; logistic regression for categorical targets) to quantify linear separability of specific grid characteristics from intermediate activations. Probe performance

is reported on held-out samples using standard metrics (e.g., R^2 for regression). Importantly, probes are trained *post hoc* on frozen activations and do not affect the underlying model.

F.2 Implicit separation of node roles

Figure 12 visualizes PCA projections of intermediate activations for samples from case118, colored by node type (bus vs. generator vs. load vs. shunt) for representative architectures: GCN (homogeneous message passing), Transformer (homogeneous attention), and HGT (heterogeneous attention with explicit typing). Two qualitative patterns are consistent with the main-paper findings.

First, HGT yields clear separation between component roles in intermediate layers, as expected given type-aware parametrization. Second, the Transformer exhibits visibly stronger clustering by node type than purely message-passing homogeneous baselines (GCN), suggesting that attention-based aggregation can learn intermediate features that reflect component roles even without explicit type-specific weights. This behavior is consistent with Transformer’s comparatively robust performance under topology shift in the main evaluation: representations that distinguish functional roles can help preserve feasibility-relevant patterns across networks.

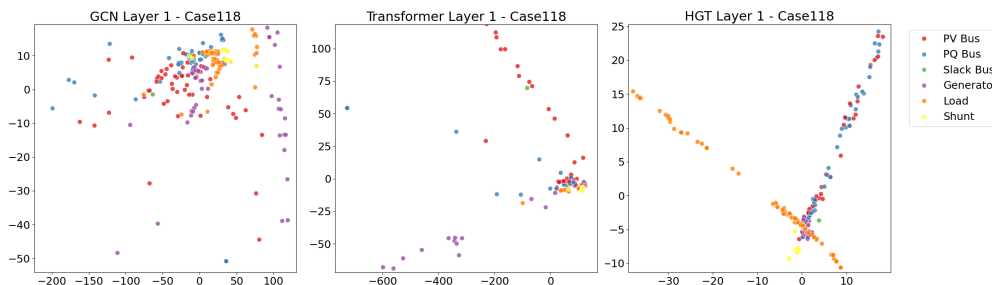


Figure 12: PCA of layer activations for samples from case118, labeled by node type, for GCN, Transformer, and HGT. The transformer model appears to implicitly encode node type information more similarly to a heterogeneous model irrespective of input types, as seen by the linear separability of node types in the model’s intermediate layers.

F.3 Effect of constraint-aware training on representation geometry

We next compare representations learned under the AL objective versus pure supervised MSE training for the same backbone (HGT). Figure 13 shows PCA projections of activations from the top convolution/attention layer for case30, with points colored by system load. Both objectives produce representations that correlate with load, indicating that the model encodes physically meaningful operating conditions. However, the AL-trained model exhibits a more curved and multi-modal structure in the projected space, while the MSE-trained model appears more linearly organized.

This qualitative difference is consistent with the role of AL: by directly penalizing feasibility residuals, AL can encourage feature transformations that separate regimes where constraints become active (e.g., near operational limits), which may not be well captured by purely accuracy-driven objectives. We emphasize that PCA is a coarse projection; the key takeaway is that constraint-aware training modifies representation geometry in ways aligned with feasibility objectives.

F.4 Layerwise linear probing: AL increases nonlinearity with depth

To quantify the preceding observation, we perform layerwise linear probing of intermediate activations with respect to system load. Figure 14 reports probe performance across HGT layers for models trained with AL and MSE. The trends suggest that AL leads to intermediate representations that become less well-explained by a linear map to load as depth increases, while still maintaining overall predictive performance in the main task. A plausible interpretation is that AL encourages progressively more abstract and nonlinear feature

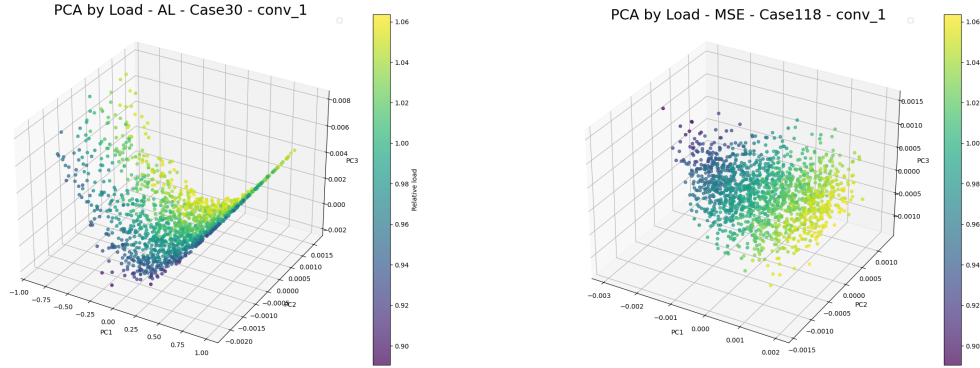


Figure 13: PCA components of activation for the top layer of convolutions in HGT trained on AL (left) vs MSE (right) losses. We see that both losses lead to the model capturing physical system load, but AL enforces a much more non-linear structure on the model’s internal representation.

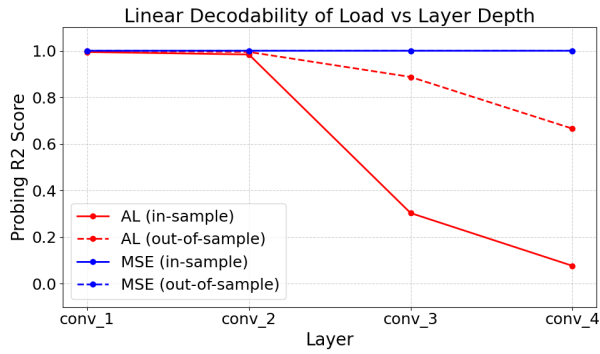


Figure 14: Linear probing of HGT layers with respect to system load. The choice of AL loss induces additional nonlinearity in the model activations without a decrease in model performance, suggesting that it encourages more abstract feature extraction by the underlying transformer as we progress through network layers.

extraction, potentially reflecting the need to represent feasibility-relevant regimes beyond a simple linear encoding of operating conditions.

We treat this analysis as supportive evidence rather than a primary claim: linear probe metrics depend on probe capacity and the specific target variable. Nevertheless, the consistent separation between AL and MSE across layers aligns with the empirical improvements in constraint satisfaction reported in the main paper.